

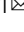


Quantum entangled fractional topology and curvatures

Joel Hutchinson ¹ & Karyn Le Hur ¹ 

Topological spaces have numerous applications for quantum matter with protected chiral edge modes related to an integer-valued Chern number, which also characterizes the global response of a spin-1/2 particle to a magnetic field. Such spin-1/2 models can also describe topological Bloch bands in lattice Hamiltonians. Here we introduce interactions in a system of spin-1/2s to reveal a class of topological states with rational-valued Chern numbers for each spin providing a geometrical and physical interpretation related to curvatures and quantum entanglement. We study a driving protocol in time to reveal the stability of the fractional topological numbers towards various forms of interactions in the adiabatic limit. We elucidate a correspondence of a one-half topological spin response in bilayer semimetals on a honeycomb lattice with a nodal ring at one Dirac point and a robust π Berry phase at the other Dirac point.

¹CPHT, CNRS, Ecole Polytechnique, Institut Polytechnique de Paris, Palaiseau, France. email: karyn.le-hur@polytechnique.edu

In recent years, rising interest in topology has traveled from mathematics to physics owing to advances in quantum science and technology. This allows for the direct observation of the Chern number distinguishing topological insulators and superconductors from their normal counterparts^{1,2}. The properties of these systems can be revealed from the reciprocal or momentum space, where the Bloch Hamiltonian maps onto the Hamiltonian of a spin-1/2 particle or two-state system in an applied magnetic field that acts radially on the Poincaré (Bloch) sphere³ with polar angle θ and azimuthal angle ϕ . Upon adiabatically sweeping from the north to south pole, along a curved path with fixed angle ϕ , the Chern number \mathcal{C} of this two-state system represented by a vector of Pauli matrices $\boldsymbol{\sigma} = (\sigma_x, \sigma_y, \sigma_z)$ is equal to 1. Incredibly, this topological quantity can be measured directly from the spin magnetizations at the poles^{4–6}

$$\begin{aligned} \mathcal{C} &\equiv \frac{1}{2\pi} \int_0^{2\pi} d\phi \int_0^\pi d\theta \mathcal{F}_{\phi\theta} \\ &= \frac{1}{2} (\langle \sigma_z(\theta=0) \rangle - \langle \sigma_z(\theta=\pi) \rangle) = 1. \end{aligned} \tag{1}$$

The angles $\theta=0$ and $\theta=\pi$ refer to the north and south poles of the sphere, respectively. We have introduced the Berry curvature

$$\mathcal{F}_{\phi\theta} \equiv \partial_\phi \mathcal{A}_\theta - \partial_\theta \mathcal{A}_\phi, \tag{2}$$

and the Berry connection \mathcal{A} , defined from the gradient of the ground state $|\psi\rangle$ according to⁷

$$\mathcal{A}_\alpha = i \langle \psi | \partial_\alpha | \psi \rangle. \tag{3}$$

The associated Berry phase represents an important foundation of quantum physics⁸. In the quantum Hall effect, such a geometrical description in terms of curvatures plays a key role in the link with electronic transport properties such as the quantum Hall conductivity^{9,10}. Here, the integer Chern number \mathcal{C} of a given spin-1/2 is related to a topological charge—the degeneracy point of the Hamiltonian—contained within the sphere spanned by the magnetic field vector. The spin-1/2 orientation then measures directly this topological charge^{11–13}. A recent experiment¹² has studied two spin-1/2s, σ_1 and σ_2 , under the influence of the radial fields \mathbf{H}_1 and \mathbf{H}_2 forming the surface of the sphere. The two spins interact through a transverse coupling ($\sigma_1^x \sigma_2^x + \sigma_1^y \sigma_2^y$). Their resulting topological phase diagram consists of integer $\mathcal{C} = 0, 1$, and 2 phases, corresponding to topological charges located outside both spheres, inside one sphere, and inside both spheres, respectively. To show the possibility of entangled states with a stable fractional Chern number for each spin, we add a crucial ingredient corresponding to adjustable constant magnetic fields on the sphere. In the following, we introduce a model with two spins $\boldsymbol{\sigma}^1 = (\sigma_1^x, \sigma_1^y, \sigma_1^z)$ and $\boldsymbol{\sigma}^2 = (\sigma_2^x, \sigma_2^y, \sigma_2^z)$ interacting through an Ising coupling, to reveal half-topological numbers for each spin on the sphere. The topology is defined on each subsystem, here a spin-1/2, directly from the poles. We show applications of the spheres with $\mathcal{C} = 1/2$ per spin for the characterization of topological semimetallic phases in bilayer honeycomb systems showing one Dirac point associated with a π Berry phase and another Dirac point revealing a nodal entangled ring. We generalize the effect including XY couplings and higher numbers of spins.

Results

Model with two spheres. The Hamiltonian for two spheres reads

$$\mathcal{H}^\pm = -(\mathbf{H}_1 \cdot \boldsymbol{\sigma}^1 \pm \mathbf{H}_2 \cdot \boldsymbol{\sigma}^2) \pm \tilde{r}f(\theta) \sigma_z^1 \sigma_z^2. \tag{4}$$

The magnetic field \mathbf{H}_i acts on the same sphere parameterized by (θ, ϕ) and may be distorted along the \hat{z} direction with the

addition of the uniform field M_i according to⁴

$$\mathbf{H}_i = (H \sin \theta \cos \phi, H \sin \theta \sin \phi, H \cos \theta + M_i), \tag{5}$$

for $i = 1, 2$. We show below through energetics arguments that the fields M_i are indeed important to stabilize a fractional Chern number. We also consider a generic θ -dependent coupling $\tilde{r}f(\theta)$ with $\tilde{r}f(\theta) > 0$. The \pm denotes two distinct classes of models. It is important to highlight here that in the case where a spin-1/2 is coupled to an environment, the topological number associated with the spin may vary continuously from $\mathcal{C} = 1$ to $\mathcal{C} = 0$ dependently on the coupling strength between the two systems. In the present case, we show that the fractional Chern numbers are stable toward smooth deformations of the geometry and toward the form of the interactions. In experiments, the magnetizations may be measured for each spin independently, such that the Chern number also has a well-defined component corresponding to each subsystem. Therefore, we find it important to first generalize Eqs. (1) and (3) for subsystem or spin j in the interacting model. The corresponding Chern number \mathcal{C}^j will provide a robust topological number related to the quantum Hall conductivity and will also represent a measure of entanglement. The spin system we consider here provides a nice platform for understanding how topology can be partitioned between subsystems.

While the eigenstates of the Hamiltonian (4) are in general complicated for $\tilde{r}f(\theta) \neq 0$, their ϕ -dependence is very simple, such that the ground state wavefunction of the system can be written as $|\psi\rangle = \sum_{kl} c_{kl}(\theta) |\Phi_k(\phi)\rangle_1 |\Phi_l(\phi)\rangle_2$. In the standard representation of a single-spin eigenstate in a radial magnetic field, the ground state is $|\uparrow\rangle$ at the north pole where $\theta = 0$, and $e^{i\phi} |\downarrow\rangle$ at the south pole where $\theta = \pi$. We will take these states to form our single-spin basis and introduce the standard spin or representation, $|\Phi_+(\phi)\rangle_j = |\uparrow\rangle = \begin{pmatrix} 1 \\ 0 \end{pmatrix}$ and $|\Phi_-(\phi)\rangle_j = e^{i\phi} |\downarrow\rangle = \begin{pmatrix} 0 \\ e^{i\phi} \end{pmatrix}$ for the two spins with $j = 1, 2$. Therefore, in the wavefunction we have $k, l = \pm$.

For $\tilde{r} \rightarrow 0$ and $M_i \rightarrow 0$, the ground state $|\psi\rangle$ then shows $c_{++}(\theta) = \cos^2 \frac{\theta}{2}$, $c_{--}(\theta) = \sin^2 \frac{\theta}{2}$, and $c_{+-}(\theta) = c_{-+}(\theta) = \sin \frac{\theta}{2} \cos \frac{\theta}{2}$ with the normalization equation $\sum_{kl} |c_{kl}|^2 = 1$ where $k, l = \pm$. While there are many ways to represent these single-spin states, their relative phase $e^{i\phi}$ is fixed. At a general level, we have $c_{kl}(\theta) = c_{kl}^1(\theta) c_{kl}^2(\theta)$ such that the wavefunction of the system can be equivalently written as $|\psi\rangle = \sum_{kl} |c_{kl}^1(\theta)\Phi(\phi)_k\rangle_1 |c_{kl}^2(\theta)\Phi(\phi)_l\rangle_2$. Then, we introduce the partial derivative symbol ∂_α^1 , which equally refers to $\partial_\alpha^1 \mathbb{I} \otimes \mathbb{I}$ when applied on $|\psi\rangle$, where 2×2 identity matrices \mathbb{I} mean that the partial derivative acts identically on the two components of a spin-1/2 spin or and through the direct product it acts on the subspace of one spin-1/2 only (here the first spin). We introduce a similar definition for ∂_α^2 as $\mathbb{I} \otimes \partial_\alpha^2 \mathbb{I}$ acting on the second spin-1/2. The Berry connection for the j th spin is then naturally defined as $\mathcal{A}_\alpha^j \equiv i \langle \psi | \partial_\alpha^j | \psi \rangle$ where $\alpha = \phi, \theta$, along with the j th Berry curvature $\mathcal{F}_{\phi\theta}^j = \partial_\phi^j \mathcal{A}_\theta^j - \partial_\theta^j \mathcal{A}_\phi^j$, and Chern number

$$\mathcal{C}^j = \frac{1}{2\pi} \int_0^{2\pi} d\phi \int_0^\pi d\theta \mathcal{F}_{\phi\theta}^j. \tag{6}$$

The operator ∂_α^j acts on the Hilbert space of the j th spin. Here, \mathcal{A}_θ^j is not uniquely defined, but \mathcal{C}^j still is since $\mathcal{A}_\theta^j = i \sum_{kl} c_{kl}^*(\theta) \partial_\theta^j c_{kl}(\theta)$ with $\partial_\theta^1 c_{kl}(\theta) = c_{kl}^2(\theta) (\partial_\theta c_{kl}^1(\theta))$ and $\partial_\theta^2 c_{kl}(\theta) = c_{kl}^1(\theta) (\partial_\theta c_{kl}^2(\theta))$, so that we can safely summarize that $\partial_\phi^j \mathcal{A}_\theta^j = 0$. From the relations $\partial_\phi^j |\Phi_-(\phi)\rangle_j = i |\Phi_-(\phi)\rangle_j$ and $\partial_\phi^j |\Phi_+(\phi)\rangle_j = 0$, the Berry connection then reads: $\mathcal{A}_\phi^1 =$

$-|c_{+-}(\theta)|^2 - |c_{--}(\theta)|^2$ and $\mathcal{A}_\phi^2 = -|c_{+-}(\theta)|^2 - |c_{--}(\theta)|^2$. Note that product states such as $|\uparrow\rangle_1|\uparrow\rangle_2$ or $|\downarrow\rangle_1|\downarrow\rangle_2$ will contribute 0 or -1 to the Berry connection, while a maximally entangled Einstein–Podolsky–Rosen or Bell state¹⁴, such as $\frac{1}{\sqrt{2}}(|\uparrow\rangle_1|\downarrow\rangle_2 + |\downarrow\rangle_1|\uparrow\rangle_2)$, will give $-1/2$.

From Eq. (6), the Chern number for the j th spin can be written as

$$\mathcal{C}^j = -(\mathcal{A}_\phi^j(\pi) - \mathcal{A}_\phi^j(0)). \quad (7)$$

Additional derivations of this are shown in Supplementary Note 1 through Stokes’ theorem and the introduction of smooth fields. It is interesting to observe that a similar correspondence is useful to describe the “quantized” topological response of one pseudospin-1/2 when coupling with circularly polarized light then referring to quantized circular dichroism of light^{15–17}. Here, we also show that Eq. (7) defining the topology at the poles only is related to the charge polarization and the quantum Hall conductivity for the subsystem j itself, see Supplementary Note 1. Then, we have the general result

$$\begin{aligned} \mathcal{C}^1 &= |c_{+-}(\pi)|^2 + |c_{--}(\pi)|^2 - |c_{+-}(0)|^2 - |c_{--}(0)|^2, \\ \mathcal{C}^2 &= |c_{+-}(\pi)|^2 + |c_{--}(\pi)|^2 - |c_{+-}(0)|^2 - |c_{--}(0)|^2. \end{aligned} \quad (8)$$

From the Pauli operator $\sigma_z^j = |\uparrow\rangle_{jj}\langle\uparrow| - |\downarrow\rangle_{jj}\langle\downarrow|$ and from the normalization equation of the state $|\psi\rangle$, we also find the equality $\langle\psi|\sigma_z^j|\psi\rangle = 1 + 2\mathcal{A}_\phi^j$, leading to

$$\mathcal{C}^j = \frac{1}{2}(\langle\sigma_z^j(\theta=0)\rangle - \langle\sigma_z^j(\theta=\pi)\rangle). \quad (9)$$

Equation (9) is an interesting generalization of Eq. (1) because this shows that one can yet define and measure for these interacting models in curved space the topology from the magnetizations of a given spin j at the poles.

Now, we consider the specific system of interest whose ground state evolves from a product state at $\theta = 0$ to an entangled state at $\theta = \pi$

$$|\uparrow\rangle_1|\uparrow\rangle_2 \rightarrow \frac{1}{\sqrt{2}}(|\uparrow\rangle_1|\downarrow\rangle_2 + |\downarrow\rangle_1|\uparrow\rangle_2). \quad (10)$$

The nonzero coefficients are $|c_{++}(0)|^2 = 1$ and $|c_{+-}(\pi)|^2 = |c_{-+}(\pi)|^2 = \frac{1}{2}$, for which

$$\mathcal{C}^1 = \mathcal{C}^2 = \frac{1}{2}. \quad (11)$$

The presence of entanglement at one pole leads to a fractional Chern number of 1/2 for each spin. This value is in agreement with $\langle\sigma_z^j(\theta=0)\rangle = 1$ and with $\langle\sigma_z^j(\theta=\pi)\rangle = 0$, reflecting the formation of a maximally entangled Bell pair at the south pole¹⁴. The norm of each spin effectively shrinks at the south pole, leading to a $\ln 2$ entanglement entropy¹⁸. In the case where the two spins would form a product state that follows the magnetic field, then from $c_{++}(0) = 1$ and $c_{--}(\pi) = 1$, we verify $\mathcal{C}^j = 1$. In the case where the two spins would be entangled at both poles then $\mathcal{C}^j = 0$.

To show that our model in Eq. (4) does indeed fulfill the necessary prerequisites to observe $\mathcal{C}^1 = \mathcal{C}^2 = \frac{1}{2}$, we study the topological phase diagram which is entirely determined by the energetics at the poles. For clarity, we analyze the \mathcal{H}^+ Hamiltonian, hereafter the \mathcal{H}^- Hamiltonian, reveals a similar fractional phase. At the poles, the ground state is readily determined, and the resulting topological phase for each spin is shown in Fig. 1a for a constant interaction $f(\theta) = 1$. Allowing for a nonconstant interaction does not change this phase diagram significantly, though it does open up the intriguing possibility of a

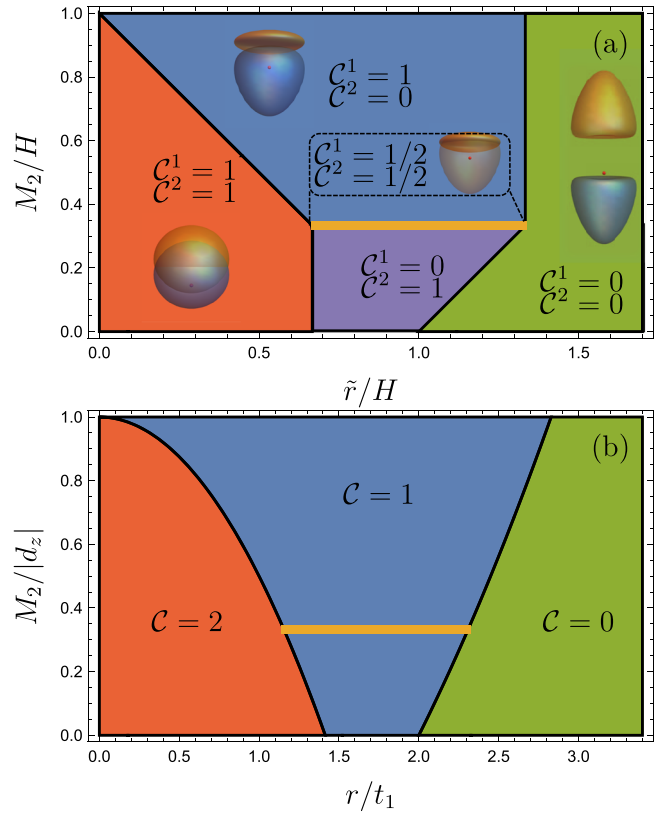


Fig. 1 Topological phase diagrams. **a** Spin-1/2 model: topological phase diagram for each spin in the $(M_2/H, \tilde{r}/H)$ plane where M_2 is the bias field on the second qubit, \tilde{r} is the interaction, and H is the radial magnetic field. Lines demarcate regions of different partial Chern numbers. Here, we have set the bias field for the first qubit to $M_1 = H/3$. The gold line at $M_2 = M_1$ indicates the symmetric phase with partial Chern numbers $\mathcal{C}^1 = \mathcal{C}^2 = \frac{1}{2}$. The insets illustrate (adiabatically deformed) spheres corresponding to the parameter space spanned by the effective field for spin 1 (blue) and spin 2 (orange) in each phase. The topological charge at the origin is indicated by the red dot. Along the gold line the effective-field manifold (which is identical for each spin) is in a coherent superposition of containing and not containing the monopole yielding a Chern number of 1/2 for each spin. **b** Lattice model: topological phase diagram in the (M_2, r) plane for the total Chern number at half-filling, defined with the two lowest occupied bands. Here, M_2 refers to the Semenoff mass in layer 2 and r is the interlayer hopping. The gold line at $M_2 = M_1$ indicates the symmetric phase for which the gap is closed. t_1 is the nearest-neighbor hopping amplitude, and $|d_z| = 3\sqrt{3}t_2$ is the next-nearest-neighbor amplitude at the Dirac points.

direct transition from $\mathcal{C}^1 + \mathcal{C}^2 = 2$ to $\mathcal{C}^1 + \mathcal{C}^2 = 0$ at the solution of $(H - M_2)/f(\pi) = \tilde{r} = (H + M_1)/f(0)$.

In the presence of \mathbb{Z}_2 symmetry between the two spins corresponding to $\sigma_z^1 \leftrightarrow \sigma_z^2$ when $M_1 = M_2 \equiv M$ in Eq. (4), the ground state at the north pole with $\theta = 0$, is $|\uparrow\rangle_1|\uparrow\rangle_2$ provided that $\tilde{r}f(0) < H + M$. At the south pole with $\theta = \pi$, the ground state is $|\downarrow\rangle_1|\downarrow\rangle_2$ for $\tilde{r}f(\pi) < H - M$, but it is degenerate between the antialigned configurations for $\tilde{r}f(\pi) > H - M$. In that case, the presence of the transverse fields in the Hamiltonian along the path over the sphere will then produce the analog of resonating valence bonds¹⁹. Indeed in this section, we will see that the singlet state is decoupled from the rest, while the triplet state $\frac{1}{\sqrt{2}}(|\uparrow\rangle_1|\downarrow\rangle_2 + |\downarrow\rangle_1|\uparrow\rangle_2)$, showing the resonance between the two valence bond states $|\uparrow\rangle_1|\downarrow\rangle_2$ and $|\downarrow\rangle_1|\uparrow\rangle_2$, is the one

adiabatically connected to the $\theta = 0$ ground state. As a result, we obtain half-integer Chern numbers (Eq. 11). For the simple constant interaction $f(\theta) = 1$, this occurs within the range

$$H - M < \tilde{r} < H + M, \quad (12)$$

indicated by the gold line in Fig. 1a. This line can be considered as a critical point between two distinct topological phases of a given spin. In the limit $M \rightarrow 0$, it becomes the quantum critical point between the total Chern number 2 and total Chern number 0 phases. We find that the \mathcal{H}^- Hamiltonian also contains a line of fractional Chern numbers with $\mathcal{C}^1 = -\mathcal{C}^2 = \frac{1}{2}$. In Supplementary Note 2, we show that the fractional phase with $\mathcal{C}^j = 1/2$ can be stabilized and in fact spreads in the presence of an XY coupling.

We also verify that the fractional Chern number may be generalized for $N > 2$ spins; starting from a product state at the north pole, spins may evolve via the transverse field to an entangled state at the south pole with $\mathcal{C}^j = 1/2$ for an even number of spins or $\mathcal{C}^j = \frac{N+1}{2N}$ for a frustrated system with an odd number of spins. See Supplementary Note 3. The spin model of Supplementary Fig. 3b, at the south pole, can be mapped onto the same Majorana fermions as in the Kitaev spin ladder geometry²⁰ through the Jordan–Wigner transformation, providing a relation between \mathbb{Z}_2 gauge theories and $\mathcal{C}^j = 1/2$ for $N = 4$ spins.

Geometrical interpretation. There is another geometric picture we can use to understand the topological nature of these numbers. For a spin-1/2 system, the Chern number counts the number of degeneracy monopoles associated with the topological charges contained within the closed manifold spanned by the magnetic field, in accordance with Gauss’ law²¹. We can adapt this picture to the case of interacting spins, where the effective magnetic field for each spin depends on the orientation of the other. In a mean-field sense, this would amount to $\mathbf{H}_1^{\text{eff}} = -\mathbf{H}_1 + \tilde{r}f(\theta)(\sigma_z^2)\hat{z}$ with \hat{z} a unit vector along the z axis. Each of the two manifolds spanned by $\mathbf{H}_1^{\text{eff}}, \mathbf{H}_2^{\text{eff}}$ may or may not contain the degeneracy monopole as illustrated by the insets in Fig. 1a, resulting in the different possibilities of $\mathcal{C}_i = 0, \pm 1$. Thus, \mathcal{C}_i , which counts the topological charge of the effective model describing the subsystem, is robust against local perturbations of the effective field. For the entangled case, the manifold spanned by the effective magnetic field on each spin rather consists of a coherent superposition of two geometries: the one that contains the monopole and the one that does not, represented schematically by the inset corresponding to the gold line in Fig. 1a. From Stokes’ theorem, the geometry (hemisphere) encircling the topological charge can be related to a pole associated with a π Berry phase, see Eq. (33) of Supplementary Note 1. The correspondence for the two spins is also similar to having two tori placed one on top of the other; when switching on the interaction, the topological response for each subsystem becomes equivalent to having a half torus encircling a hole and the remaining surface participating in the quantum entanglement.

Now, we show that this spin-1/2 model can also find applications in topological lattice models. It is well known that the Haldane model²²—a two-dimensional Chern insulator which has been realized in quantum materials²³, graphene²⁴, cold atoms^{25,26} and light systems^{27–31}—has a natural pseudospin-1/2 representation due to the A and B sublattices of the honeycomb lattice where the Brillouin zone torus can be mapped onto the parameter space discussed above. It follows that a stack of two Haldane layers may be represented by a two-spin model.

Lattice model. We consider a plane realization of Eq. (4) consisting of two AA and BB -stacked graphene lattices³² and show

how to find a fractional magnetization representing \mathcal{C}^j . Here, $\theta = 0$ and $\theta = \pi$ map onto the K and K' points of the first Brillouin zone, respectively (see Supplementary Note 4). The spin degrees of freedom now describe the momentum-space sublattice magnetization for each layer j . A correspondence between the spheres model and the lattice model, which will be developed below Eq. (16), can be formulated through the identification $\sigma_z^j \leftrightarrow n_{kB}^j - n_{kA}^j$. Here, $n_{k\alpha}^j$ represents the density of particles associated with sublattice $\alpha = A$ or B for a wavevector \mathbf{k} , in a given layer j . The bilayer system is half-filled. The values M_j from the previous section now describe inversion-symmetry breaking Semenoff masses, which may be tuned for each layer³³. We highlight here that from the spheres’ formalism, the topology is introduced here through tunable Berry phases in each layer in accordance with the Haldane model. If the two layers have equal fluxes, the model corresponds to the \mathcal{H}^+ Hamiltonian, while if they have opposite fluxes, it describes the \mathcal{H}^- Hamiltonian, which is equivalent to the Kane–Mele model³⁴. Here, we will discuss the situation with equal fluxes. The mapping suggests that we need an unusual interaction—one that is local in \mathbf{k} -space—to produce a momentum-dependent Ising interaction. Such interactions have been studied in relation to Weyl semimetals^{35,36}. In fact, we can achieve the same result with an interlayer coupling r between neighboring sites. All of this motivates the following lattice model in momentum space:

$$\mathcal{H} = \sum_{\mathbf{k}} (\psi_{k1}^\dagger, \psi_{k2}^\dagger) \mathcal{H}(\mathbf{k}) \begin{pmatrix} \psi_{k1} \\ \psi_{k2} \end{pmatrix}, \quad (13)$$

where $\psi_{ki}^\dagger \equiv (c_{kAi}^\dagger, c_{kBi}^\dagger)$ and

$$\mathcal{H}(\mathbf{k}) = \begin{pmatrix} (\mathbf{d} + M_1 \hat{z}) \cdot \boldsymbol{\sigma} & r \mathbb{I} \\ r \mathbb{I} & (\mathbf{d} + M_2 \hat{z}) \cdot \boldsymbol{\sigma} \end{pmatrix} \quad (14)$$

is represented in terms of the Pauli matrices $\boldsymbol{\sigma}$, the 2×2 identity matrix \mathbb{I} , and the \mathbf{k} -dependent vector \mathbf{d} is defined in accordance with the Haldane model in each layer (see Supplementary Note section 4 for details). The indices $i = 1, 2$ indicate the layer.

The eigenvalues and eigenvectors of this matrix are readily found at the K and K' points where the gap closes, respectively, for the values of r

$$\begin{aligned} r_c^+ &\equiv \sqrt{|d_z| + M_1} \sqrt{|d_z| + M_2} \\ r_c^- &\equiv \sqrt{|d_z| - M_1} \sqrt{|d_z| - M_2}. \end{aligned} \quad (15)$$

For the case of asymmetric Semenoff masses $M_1 \neq M_2$, the gap closes and reopens at r_c^- . When $M_1 \neq M_2$, computing the Berry curvature numerically³⁷, we show in Fig. 1b that the phase diagram for the total Chern number \mathcal{C} at half-filling is defined from the two lowest occupied bands, in agreement with established results³². A topological transition takes place where the Chern number of the second band changes from 1 to 0. When the gap closes and reopens at K this number goes to -1 . The Chern number of the first band (lowest band) remains 1 throughout. The similarity between Fig. 1a and 1b suggests that there indeed exists a faithful mapping between the lattice model and the spin model, which has been shown to be certainly valid close to the transition between the phases $\mathcal{C} = 2$ and $\mathcal{C} = 1$ (starting from the $\mathcal{C} = 1$)³².

Now, we study the (gold) line $M_1 = M_2$ where the system shows an additional \mathbb{Z}_2 layer symmetry ($1 \leftrightarrow 2$) which is at the origin of the fractional Chern number. This situation describes a special class, where time-reversal and inversion symmetry are not present due to the flux and mass terms, while a \mathbb{Z}_2 symmetry is preserved. The result is a nodal ring semimetal where the second and third bands cross as shown in Fig. 2a. A time-reversal invariant version of this case has been discussed³⁸. The

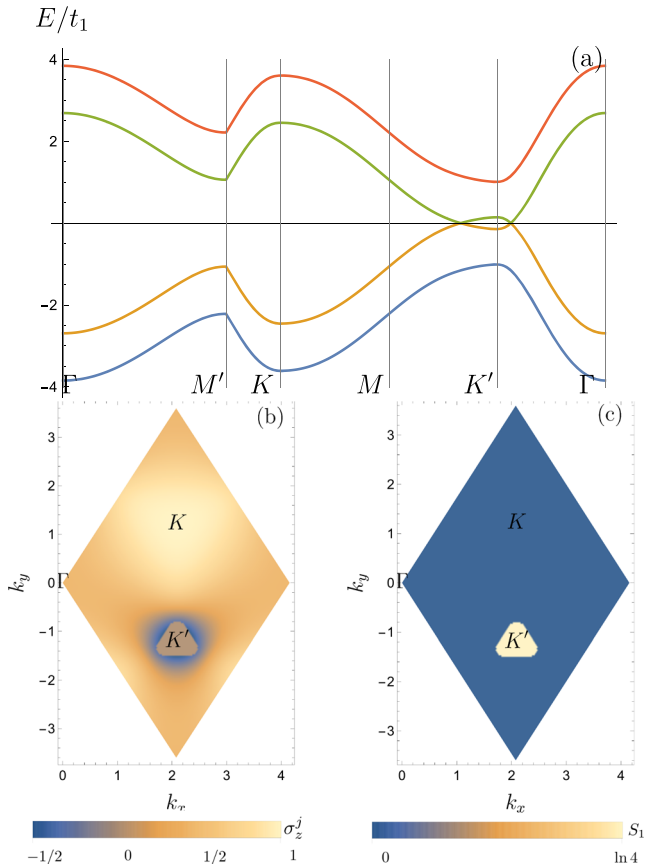


Fig. 2 Two stacked Haldane layers. **a** Bulk band structure through the high symmetry points. **b** Sublattice magnetization $\sigma_z^j \equiv \langle n_{\mathbf{k}B}^j - n_{\mathbf{k}A}^j \rangle$ in one layer over the primitive cell of the reciprocal lattice at the K Dirac point, the light yellow color refers to magnetization 1, the K' Dirac point has a magnetization equal to 0 as a result of entanglement. **c** Entanglement entropy S_1 of one layer in the same region (yellow refers to a maximum entropy of $\ln 4$ and in the blue region the entropy is 0). The parameters chosen for all panels are $|d_z| = \sqrt{3}t_1$, $r = \sqrt{3}t_1/3$ (which is in the range $r_c^- < r < r_c^+$), and $M_1 = M_2 = 3\sqrt{3}t_1/4$ (symmetric Semenoff masses). Here, t_1 is the nearest-neighbor hopping amplitude, $|d_z|$ is the next-nearest-neighbor amplitude at the Dirac points, and M_1, M_2 are the Semenoff masses in the two layers.

eigenstates at the poles take the simple form

$$\begin{aligned} \psi_1 &= \frac{1}{\sqrt{2}}(0, -1, 0, 1), & \psi_2 &= \frac{1}{\sqrt{2}}(0, 1, 0, 1), \\ \psi_3 &= \frac{1}{\sqrt{2}}(-1, 0, 1, 0), & \psi_4 &= \frac{1}{\sqrt{2}}(1, 0, 1, 0). \end{aligned} \quad (16)$$

Defining $|\psi_g\rangle \equiv \frac{1}{2}(c_{A1}^\dagger c_{B1}^\dagger - c_{A1}^\dagger c_{B2}^\dagger - c_{A2}^\dagger c_{B1}^\dagger + c_{A2}^\dagger c_{B2}^\dagger)|0\rangle$, we see that at $r = r_c^+$, there is a transition in the ground state at K from $c_{B1}^\dagger c_{B2}^\dagger|0\rangle$, with $|0\rangle$ referring to the vacuum state, to $|\psi_g\rangle$. Meanwhile at K' , there is a transition at $r = r_c^-$ from $c_{A1}^\dagger c_{A2}^\dagger|0\rangle$ (which is favored by the Semenoff masses) to $|\psi_g\rangle$ (which is favored by the interaction). Here, we develop the correspondence with the spheres model for specific values of r between r_c^- and r_c^+ such that the fractional state can occur. It is important to emphasize here that at half-filling, the two lowest-energy bands are occupied, giving rise to a two-particle wavefunction. At the K point, the ground state can be written as $c_{B1}^\dagger c_{B2}^\dagger|0\rangle = |\uparrow\uparrow\rangle$. We can then define the pseudospin magnetization in each plane as

$\sigma_z^j(K) \leftrightarrow n_B^j(K) - n_A^j(K)$ with $n_B^j = c_{Bj}^\dagger c_{Bj}$ and similarly for the sublattice A . Here, σ_z^j measures the particle-density asymmetry between sublattice A and B resolved for a k value. At the K point, populating an eigenstate $c_{A1}^\dagger c_{A2}^\dagger|0\rangle = |\downarrow\downarrow\rangle$ then requires an additional energy related to $|d_z|$. At the K' point, the nodal ring involves the state $|\psi_g\rangle$. Importantly, the states $c_{A1}^\dagger c_{B1}^\dagger|0\rangle$ and $c_{A2}^\dagger c_{B2}^\dagger|0\rangle$ do not modify the pseudospin magnetization in each plane as they favor an equal particle density on the two sublattices, but they will participate in the entanglement entropy maximum in the nodal ring region. Therefore, from the point of view of the pseudospin magnetization at the Dirac points or equivalently at the poles on the sphere, only four states intervene. Explicitly, the correspondence between states in the lattice model and states in the sphere model is given by

$$c_{B1}^\dagger c_{B2}^\dagger|0\rangle = |\uparrow\uparrow\rangle, c_{A1}^\dagger c_{A2}^\dagger|0\rangle = |\downarrow\downarrow\rangle, c_{B1}^\dagger c_{A2}^\dagger|0\rangle = |\uparrow\downarrow\rangle, c_{A1}^\dagger c_{B2}^\dagger|0\rangle = |\downarrow\uparrow\rangle. \quad (17)$$

These are the states that enter in the evaluation of the topological properties. The pseudospin magnetic structure around the K' point is therefore related to the reduced wavefunction $\frac{1}{\sqrt{2}}(c_{A1}^\dagger c_{B2}^\dagger + c_{A2}^\dagger c_{B1}^\dagger)|0\rangle$ in $|\psi_g\rangle$ which corresponds then to the same entangled state as for the two spheres around the south pole. The topological properties of this semimetal can then be described through Eqs. (7) and (9). Thus, we introduce the lattice version of \mathcal{C}^j (Eq. (9)) as

$$\tilde{\mathcal{C}}^j = \frac{1}{2} \langle n_{KB}^j - n_{KA}^j - n_{K'B}^j + n_{K'A}^j \rangle \quad (18)$$

$$= \begin{cases} 1 & r < r_c^- \\ 1/2 & r_c^- < r < r_c^+ \\ 0 & r > r_c^+, \end{cases} \quad (19)$$

where $j = 1, 2$ refers to the layer basis and the particle densities in each sublattice A or B are resolved at a given Dirac point or pole on the sphere. The magnetization for a single layer is shown over the unit cell of the reciprocal lattice in Fig. 2b.

Alternatively, we may represent the ground state at half-filling in terms of the occupancy in each layer (comprising two sublattices with a given ket $|ij\rangle$, $i + j = 1$, such that $|10\rangle$ refers to sublattice A occupancy and $|01\rangle$ to sublattice B occupancy, respectively): $|\psi\rangle = \sum_{i+j+k+l=2} c_{ijkl} |ij\rangle_1 |kl\rangle_2$, from which we get the reduced density matrix ρ_1 by tracing out the second layer. From this, the entanglement entropy is computed numerically (see Supplementary Note 4) and shown for the case of symmetric masses in Fig. 2c. For $r < r_c^-$, the entanglement entropy is identically 0. Above r_c^- , we verify that the system shows a maximum entanglement entropy of $\ln 4$ located in the band-crossing region, in agreement with the form of $|\psi_g\rangle$. One Dirac point is characterized by a nodal ring enclosing the entangled region. Since the two Dirac points map to the two poles on the spheres, this emphasizes the correspondence between the two spins and the lattice model.

We highlight here that even though we have a band-crossing effect in the nodal ring region, the spheres' formalism allows us to conclude that the topological number defined through Eq. (7) is yet applicable in this situation showing then that $\mathcal{C}^j = 1/2$ is measurable through the quantum Hall conductivity, with j referring to one layer. From Stokes' theorem on the sphere, it is important to emphasize here that the $\mathcal{C}^j = 1/2$ topological number can also be interpreted as a π Berry phase encircling just one Dirac point associated with the topology (Eq. (33) of Supplementary Note 1). Regarding the bulk-edge correspondence,

the edge spectrum in the reciprocal space produces one chiral edge mode as in the quantum Hall effect^{39–41} and in the Haldane model²². We study the edge states of this model in real space using the KWANT code⁴² and show that for $M_1 = M_2$ this mode is equally distributed between the two planes at the edges as if a charge e in the reciprocal space redistributes as two $e/2$ effective charges in real space, in agreement with the quantum Hall conductivity for $M_1 = M_2$. When we progressively deviate from the line $M_1 = M_2$, navigating in the blue $C = 1$ region of Fig. 1b, then this mode progressively redistributes in one plane only. The nodal ring gives rise to delocalized bulk gapless modes in real space, and yet the robust topology can also be measured from the particles' densities associated with each layer resolved in momentum space at the two Dirac points from Eq. (18). We also find that the layer magnetization number \tilde{C}^j varies smoothly across the transition, in contrast to the sharp change in C^j that occurred in the spin model. See Supplementary Note 4 for further details related to these facts and proofs.

Protocol in time. Here, we show the occurrence of stable half-topological numbers in a real-time protocol, in the adiabatic limit. We also illustrate energy bands interferometry effects and deviations from these rational values when increasing the speed of the protocol. One experimental protocol for measuring C^j in a spin system is to perform a linear sweep, $\theta = vt$, $t \in [0, \pi/v]$ for some velocity v , of the magnetic field along the meridian $\phi = 0$, measuring $\langle \sigma_z^j \rangle$ at the endpoints of the path¹², i.e., at the north and south poles. Any finite velocity will lead to nonadiabatic transitions via the Landau–Zener–Majorana mechanism^{43–45}, which describes a time-dependent two-state model of the form $\mathcal{H} = \lambda t \sigma_z + \Delta \sigma_x$. The amplitudes for the $|\uparrow\rangle$ and $|\downarrow\rangle$ components of the wavefunction were derived by Zener⁴³ for the asymptotic case $t \rightarrow \infty$. Here, we are actually interested in the values at $t = 0$, which are derived in the Supplementary Note 5. There we also show that the quasi-adiabatic regime of our two-spin system is described by an effective two-state Hamiltonian

$$\mathcal{H}_{\text{eff}}^+ = -[\tilde{r}f(\theta) + H \cos \theta + M]\sigma_z - \sqrt{2}H \sin \theta \sigma_x + (H \cos \theta + M)\mathbb{I}, \quad (20)$$

where the basis for the Pauli matrices is now given by two of the triplet states $(1, 0)^T = |1, 0\rangle$ and $(0, 1)^T = |1, -1\rangle$. We see that the entangled state $|1, 0\rangle$ is indeed the unique ground state at $\theta = \pi$ for \tilde{r} sufficiently large. More precisely, the window in which the ground state evolves from the product state at the north pole to the entangled state at the south pole, and therefore has $C^j = 1/2$, is given by

$$\frac{H - M}{f(\pi)} < \tilde{r} < \frac{H + M}{f(0)}. \quad (21)$$

Returning to the dynamics of Eq. (20), we expand near $\theta = \pi$, such that $t \rightarrow t - \pi/v$. With this new time variable, the important dynamics takes place near $t = 0$ such that we approximate $f(\theta) = f(\pi)$ close to the south pole. We will see that relaxing this condition does not affect the result noticeably. We then rotate the Pauli matrices about the y -axis. In the rotated basis, the effective Hamiltonian takes the Landau–Zener form, with

$$\lambda \equiv \sqrt{2}Hv, \quad \Delta = \tilde{r}f(\pi) - H + M, \quad (22)$$

and adiabaticity parameter $\gamma = \Delta^2/\lambda$. The amplitude for measuring the $|1, -1\rangle$ state is then $\frac{1}{\sqrt{2}}(A(t) - B(t))$, while the amplitude for measuring the entangled state is $\frac{1}{\sqrt{2}}(A(t) + B(t))$. The former results in $C^j = 1$, upon sweeping to the south pole (now at $t = 0$), while the latter gives $C^j = 1/2$. The value of C^j is then related to

the coefficient $A(0)$ and $B(0)$ through

$$C^j \approx \frac{3}{4} - \frac{1}{4} \text{Re}(A(0)B^*(0)). \quad (23)$$

The product $A(0)B(0)^*$ is evaluated in the Supplementary Note 5, which yields

$$C^j \approx \frac{3}{4} + \frac{\pi}{4} \text{Re} \left(e^{i3\pi/4} e^{-\gamma\pi/4} \frac{\text{sgn}(\Delta)\sqrt{\gamma}}{\Gamma(1/2 + i\gamma/4)\Gamma(1 - i\gamma/4)} \right), \quad (24)$$

in terms of the gamma function $\Gamma(z)$. We check the adiabatic limit of this formula, $v \rightarrow 0$ ($\gamma \rightarrow \infty$), and find

$$C^j \rightarrow \frac{3}{4} - \frac{1}{4} \text{sgn}(\Delta), \quad (25)$$

which gives 1 for $\tilde{r} < (H - M)/f(\pi)$ and $1/2$ for $\tilde{r} > (H - M)/f(\pi)$. We also study numerically the time evolution of the interacting spins in this protocol (Fig. 3a–d). Our analytic result for C^j is then compared with the corresponding numerical value in Fig. 3e, f. We see that this formula accurately captures the transition in C^j for small sweep velocities.

We also find, by checking many examples, that the shape of the transition is independent of the particular form of time-dependant interaction $f(\theta)$, which for small sweep velocities only shifts the transition point. This is shown in Fig. 3f where we compare the analytic approximation to the numerical solution of the Schrödinger equation for a variety of interactions. Note that the numerical results, which retain the full θ -dependence of the interaction, do not deviate much from the analytic approximation where we set $f(\theta) \approx f(\pi)$. The fact that the C^j values are robust to such changes in the form of the interactions is a result of the topological nature of the quantum system.

Lastly, we also verified that the additional fractional phases found for $N > 2$ spins are also stable from the time evolution of these models in the quantum circuit simulator Cirq⁴⁶, illustrating that these phases can indeed be seen through the action of unitary gates in a generic quantum computer, see Supplementary Note 5.

Discussion

Our analysis shows that one can realize quantum states with fractional topology from the interplay between Berry curvatures and resonating valence bond states^{19,22,47}. Entanglement between two spins can produce a Chern number of one-half for each spin. We have provided a geometrical and physical interpretation of this result through the derivation of Eq. (7). We have shown the stability of the fractional Chern number regarding various forms of interactions in the adiabatic limit. We have formulated a correspondence with topological lattice models respecting \mathbb{Z}_2 (layer) symmetry, which form nodal ring semimetals in momentum space around a Dirac point. The one-half topological number arises from a π Berry phase around the Dirac point that shows the topological band gap and also reveals one protected low-energy edge mode in the reciprocal space. This prediction can be measured from momentum-resolved tunneling, i.e., when injecting a charge e resolved in energy and wavevector⁴⁸. In real space, we verify that this mode equally redistributes between the two planes with $1/2$ probabilities as if a charge e would equilibrate as two averaged charges $e/2$ in the two layers. It is important to highlight here that for $M_1 = M_2$, in the presence of a band-crossing effect around the nodal semimetallic ring, we have shown that the one-half topology of each spin or each plane in the bilayer model can be defined from the spin magnetizations at the poles, the bulk charge polarization, and the quantum Hall conductivity which can also be reinterpreted as an effective charge $e/2$. Since the ground state wavefunction is a direct product state on the sphere, defining the operator $\tilde{C}^j = 1/2(\sigma_z^j(0) - \sigma_z^j(\pi))$, we obtain the standard

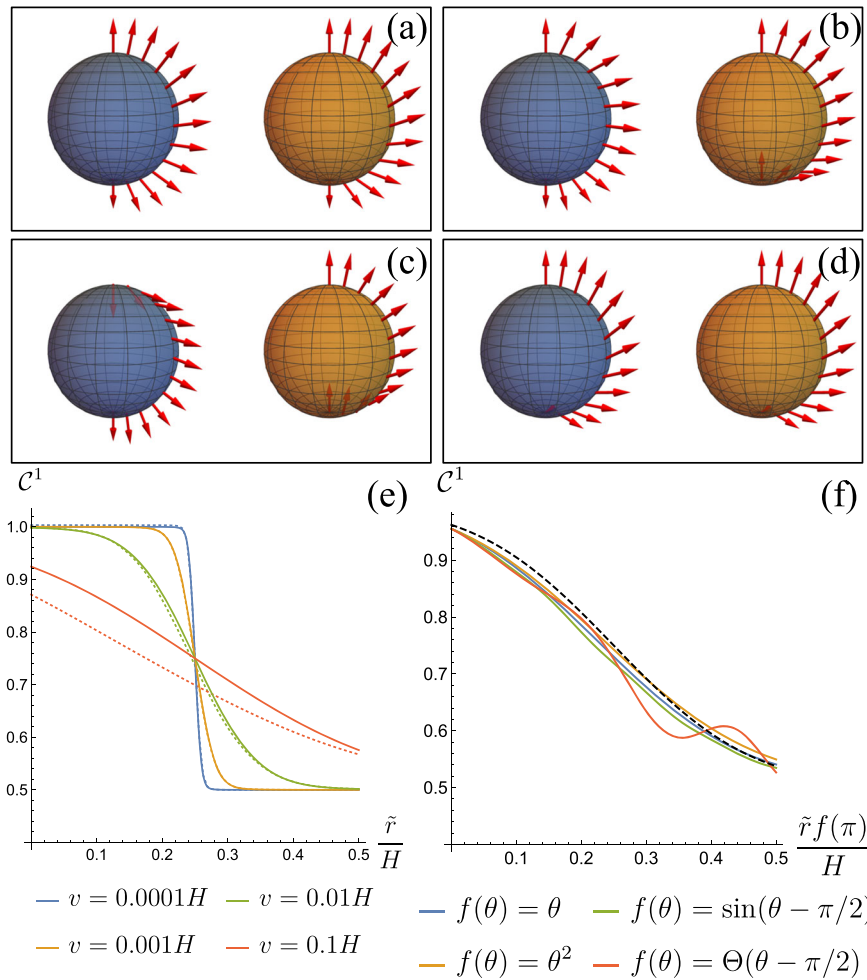


Fig. 3 Time evolution for interacting spin-1/2s. a-d Spin responses $\langle \sigma^1 \rangle$ (on the blue sphere) and $\langle \sigma^2 \rangle$ (on the orange sphere) to a sweep protocol of the radial applied magnetic field along a meridian of the sphere with sweep velocity $v = 0.0001H$. The time-dependent spin vectors shown in red are determined from the numerical solution of the Schrödinger equation. The radius of each sphere is the magnetic field strength H . **a-c** An asymmetric case where the bias fields for the two qubits are $M_1 = H/3$ and $M_2 = H/2$. The Ising couplings between the qubits are given by **(a)** $\tilde{r} = 0.25H$. **b** $\tilde{r} = 0.9H$. **c** $\tilde{r} = 1.7H$. **d-f** show the symmetric case with $M_1 = M_2 = 3H/4$. **d** Spin response for $\tilde{r} = H/3$. In this case, the magnitude of the spin vector vanishes at the south pole. **e** Chern number of a single spin versus the normalized coupling \tilde{r}/H for different sweep velocities v (shown in different colors) with interaction coefficient $f(\theta) = 1$. The solid lines show the analytic approximation of Eq. (24), while the dotted lines show the result from the numerical solution to the Schrödinger equation. **f** Numerically determined Chern number of a single spin vs $\tilde{r}f(\pi)/H$ shown by the solid lines for different interactions with $v = 0.05H$; Θ refers to the Heaviside step function. The dashed black line shows the analytic approximation of Eq. (24) which is universal for a given speed v .

deviation $e\delta\mathcal{C}^j = e\sqrt{\langle (\hat{C}^j)^2 \rangle - \langle \hat{C}^j \rangle^2} = (e/2)\sqrt{F} = e/2$ and $F = \langle \sigma_z^j(\pi)^2 \rangle - \langle \sigma_z^j(\pi) \rangle^2 = 1$, which is a result of the formation of an entangled Bell pair at the south pole. Related to circular dichroism of light, we have verified that at the topological Dirac point the response is similar to the Haldane model^{15,16} and that in the semimetallic region there is no light response, such that when averaging on both light polarizations the response at the two Dirac points is also in agreement with a one-half topological number. Increasing the number of spins can give access to other rational topological numbers as well, in relation with various forms of entangled states. These predictions can be measured with actual developments on quantum systems, entanglement, and light-matter coupling. The interpretation of this phase needs to be further studied in relation with the classification table^{21,38}, as well as interaction effects on the lattice directly from the reciprocal space^{15,35,36}. These spheres' models may also find applications as light emitters through a quantum dynamo effect⁴, many-body synchronization sources⁴⁹, and can be generalized to superconducting systems through the Nambu basis and in networks

similar to the Affleck–Kennedy–Lieb–Tasaki architecture⁵⁰ for quantum algorithms purposes.

Methods

The methodology begins from general quantum arguments to show the possibility of a fractional Chern number for an interacting spin-1/2 particle, leading to Eqs. (7), (9), and (11). Then, we analyze the ground state energetics of a particular model and show how to observe a Chern number 1/2. We justify the results from the superposition of two geometries, one encircling the topological charge and one forming the quantum entanglement. Furthermore, we formulate a mathematical correspondence between the spin-1/2 and topological bilayer lattice models. We find a relation between the Chern number measurement and the quantum Hall conductivity, the polarization, and the light response in a given plane. We perform numerical evaluations in the bilayer model of the Berry curvature, magnetization, entanglement entropy, as well as the band structure in a finite and infinite system. For the time-dependent protocol, we check, through numerical evaluation of the Schrödinger equation, that our results are very similar for various forms of spin interaction in curved space. We also study the effect of increasing the speed of the protocol related to Landau–Zener–Majorana interferometry effects.

In Supplementary Note 1, we present in the first section two proofs for the gauge invariance of Eq. (7) and show from the smooth fields that it is related to a quantum Hall conductivity $\sigma_{xy} = \frac{1}{2} \frac{e^2}{h}$ on one plane and to a π Berry phase around one Dirac point. We also discuss applications to the class of wavefunctions we study. In Supplementary Note 2, we consider generalized models with transverse coupling. In

Supplementary Note 3, we study models with higher numbers of spins. In Supplementary Note 4, we show definitions on the Haldane model and bilayer system, develop the notations for the entanglement entropy calculation, and show the edge modes and local density of states of a ribbon geometry. Lastly, in Supplementary Note 5, we present results on the time evolution of the systems. We derive the transition amplitudes for the time-dependent protocol associated with the Landau–Zener–Majorana dynamics. We also verify the possibility of other fractional topological states in time for the situation with $N > 2$ spins using the Cirq algorithm⁴⁶.

Data availability

All relevant data are available from the authors.

Code availability

All codes used to generate figures are available from the authors upon request.

Received: 22 December 2020; Accepted: 24 May 2021;

Published online: 22 June 2021

References

- Hasan, Z. & Kane, C. L. Colloquium: topological insulators. *Rev. Mod. Phys.* **82**, 3045 (2010).
- Liang Qi, X. & Zhang, S. Topological insulators and superconductors. *Rev. Mod. Phys.* **83**, 1057 (2011).
- Schleich, W. P. *Quantum Optics in Phase Space* (John Wiley & Sons, 2011).
- Henriet, L., Sclocchi, A., Orth, P. P. & Le Hur, K. Topology of a dissipative spin: dynamical chern number, bath-induced nonadiabaticity, and a quantum dynamo effect. *Phys. Rev. B* **95**, 054307 (2017).
- Gritsev, V. & Polkovnikov, A. Dynamical quantum Hall effect in the parameter space. *Proc. Natl Acad. Sci. USA* **109**, 6457–6462 (2012).
- De Grandi, C. & Polkovnikov, A. *Adiabatic Perturbation Theory: From Landau–Zener Problem to Quenching Through a Quantum Critical Point* 75–114 (Springer, 2010).
- Berry, M. V. Quantal phase factors accompanying adiabatic changes. *Proc. R. Soc. A Math. Phys. Sci.* **392**, 45–57 (1984).
- Leek, P. J. et al. Observation of berry’s phase in a solid-state qubit. *Science* **318**, 1889–1892 (2007).
- Thouless, D., Kohmoto, M., Nightingale, M. P. & den Nijs, M. Quantized Hall conductance in a two-dimensional periodic potential. *Phys. Rev. Lett.* **49**, 405 (1982).
- Haldane, F. D. M. Geometrical description of the fractional quantum Hall effect. *Phys. Rev. Lett.* **107**, 116801 (2011).
- Schroer, M. D. et al. Measuring a topological transition in an artificial spin-1/2 system. *Phys. Rev. Lett.* **113**, 050402 (2014).
- Roushan, P. et al. Observation of topological transitions in interacting quantum circuits. *Nature* **515**, 241–244 (2014).
- Körber, S., Privitera, L., Budich, J. C. & Trauzettel, B. Interacting topological frequency converter. *Phys. Rev. Res.* **2**, 022023 (2020).
- Bell, J. S. On the Einstein Podolsky Rosen paradox. *Physics* **1**, 195–200 (1964).
- Klein, P., Grushin, A. & Le Hur, K. Interacting stochastic topology and Mott transition from light response. *Phys. Rev. B* **103**, 035114 (2021).
- Tran, D. T., Dauphin, A., Grushin, A. G., Zoller, P. & Goldman, N. Probing topology by “heating”: quantized circular dichroism in ultracold atoms. *Sci. Adv.* **3**, e1701207 (2017).
- Asteria, L. et al. Measuring quantized circular dichroism in ultracold topological matter. *Nat. Phys.* **15**, 449 (2017).
- Neill, C. et al. Ergodic dynamics and thermalization in an isolated quantum system. *Nat. Phys.* **1**, 1037–1041 (2016).
- Anderson, P. W. Resonating valence bonds: a new kind of insulator? *Mater. Res. Bull.* **8**, 153–160 (1973).
- Le Hur, K., Soret, A. & Yang, F. Majorana spin liquids, topology, and superconductivity in ladders. *Phys. Rev. B* **96**, 205109 (2017).
- Bernevig, B. A. & Hughes, T. L. *Topological Insulators and Topological Superconductor* (Princeton Univ. Press, 2013).
- Haldane, F. D. M. Model for a quantum Hall effect without landau levels: condensed-matter realization of the “parity anomaly”. *Phys. Rev. Lett.* **61**, 2015–2018 (1988).
- Liu, C.-X., Zhang, S.-C. & Qi, X.-L. The quantum anomalous Hall effect. *Annu. Rev. Condens. Matter Phys.* **7**, 301–321 (2016).
- McIver, J. W. et al. Light-induced anomalous Hall effect in graphene. *Nat. Phys.* **16**, 38–41 (2020).
- Jotzu, G. et al. Experimental realization of the topological haldane model with ultracold fermions. *Nature* **515**, 237–240 (2014).
- Flaschner, N. et al. Experimental reconstruction of the berry curvature in a floquet bloch band. *Science* **352**, 1091–1094 (2016).
- Haldane, F. D. M. & Raghu, S. Possible realization of directional optical waveguides in photonic crystals with broken time-reversal symmetry. *Phys. Rev. Lett.* **100**, 013904 (2008).
- Lu, L., Joannopoulos, J. D. & Soljacic, M. Topological photonics. *Nat. Photonics* **8**, 821–829 (2014).
- Koch, J., Houck, A. A., Le Hur, K. & Girvin, S. M. Time-reversal-symmetry breaking in circuit-qed-based photon lattices. *Phys. Rev. A* **82**, 043811 (2010).
- Le Hur, K. et al. Many-body quantum electrodynamics networks: Non-equilibrium condensed matter physics with light. *Comptes Rendus Phys.* **17**, 808–835 (2016).
- Ozawa, T. et al. Topological photonics. *Rev. Mod. Phys.* **91**, 015006 (2019).
- Cheng, P. et al. Topological proximity effects in a haldane graphene bilayer system. *Phys. Rev. B* **100**, 081107 (2019).
- Semenoff, G. W. Condensed-matter simulation of a three-dimensional anomaly. *Phys. Rev. Lett.* **53**, 2449–2452 (1984).
- Kane, C. L. & Mele, E. Quantum spin Hall effect in graphene. *Phys. Rev. Lett.* **95**, 226801 (2005).
- Morimoto, T. & Nagaosa, N. Weyl Mott insulator. *Sci. Rep.* **6**, 19853 (2016).
- Meng, T. & Budich, J. C. Unpaired weyl nodes from long-ranged interactions: fate of quantum anomalies. *Phys. Rev. Lett.* **122**, 046402 (2019).
- Fukui, T., Hatsugai, Y. & Suzuki, H. Chern numbers in discretized brillouin zone: efficient method of computing (spin) Hall conductances. *J. Phys. Soc. Jpn.* **74**, 1674–1677 (2005).
- Young, S. M. & Kane, C. L. Dirac semimetals in two dimensions. *Phys. Rev. Lett.* **115**, 126803 (2015).
- Klitzing, K. V., Dorda, G. & Pepper, M. New method for high-accuracy determination of the fine-structure constant based on quantized Hall resistance. *Phys. Rev. Lett.* **45**, 494–497 (1980).
- Halperin, B. I. Quantized Hall conductance, current-carrying edge states, and the existence of extended states in a two-dimensional disordered potential. *Phys. Rev. B* **25**, 2185 (1982).
- Büttiker, M. Absence of backscattering in the quantum Hall effect in multiprobe conductors. *Phys. Rev. B* **38**, 9375 (1988).
- Groth, C. W., Wimmer, M., Akhmerov, A. R. & Waintal, X. Kwant: a software package for quantum transport. *New J. Phys.* **16**, 063065 (2014).
- Zener, C. & Fowler, R. H. Non-adiabatic crossing of energy levels. *Proc. R. Soc. A, Math. Phys. Eng. Sci.* **137**, 696–702 (1932).
- Landau, L. Zur theorie der energieübertragung i. *Z. Sowjetunion* **1**, 88–95 (1932).
- Majorana, E. Atomi orientati in campo magnetico variabile. *Il Nuovo Cim.* **9**, 43–50 (1932).
- Contributors, T. C. Cirq, a python framework for creating, editing, and invoking noisy intermediate scale quantum (nisq) circuits. Cirq Developers. (2021, May 11). Cirq (Version v0.11.0). Zenodo. <https://doi.org/10.5281/zenodo.4750446>.
- Kalmeyer, V. & Laughlin, R. B. Equivalence of the resonating-valence-bond and fractional quantum Hall states. *Phys. Rev. Lett.* **59**, 2095 (1987).
- Steinberg, H. et al. Charge fractionalization in quantum wires. *Nat. Phys.* **4**, 116–119 (2008).
- Pizzi, A., Dolcini, F. & Le Hur, K. Quench-induced dynamical phase transitions and pi-synchronization in the bose-hubbard model. *Phys. Rev. B* **99**, 094301 (2019).
- Affleck, I., Kennedy, T., Lieb, E. H. & Tasaki, H. Rigorous results on valence-bond ground states in antiferromagnets. *Phys. Rev. Lett.* **59**, 799 (1987).

Acknowledgements

The authors acknowledge discussions with Monika Aidelsburger, Kamel Hachour, Loic Henriet, Loic Herviou, Philipp Klein, and Joseph Maciejko and discussions related to presentations at Cambridge and Lisbon. K.L.H. also acknowledges discussions with students in the physics–mathematics class PHY105 and solid-state physics class PHY552A at Ecole Polytechnique, and quantum classes both at Ecole Polytechnique and Yale. This work was supported jointly by the Natural Sciences and Engineering Research Council of Canada (NSERC) as well as the French ANR BOCA (both authors). The research on lattices and ultra-cold atoms was funded by the Deutsche Forschungsgemeinschaft (DFG, German Research Foundation) via Research Unit FOR 2414 under project number 277974659 (K.L.H.). K.L.H. also acknowledges funding from NSF in USA, through DMR-0803200 on Entanglement Theory in Many-Body Quantum Systems.

Author contributions

The idea of fractional topology on the sphere and relations to observables came to K.L.H. when teaching the mathematics–physics classes at Ecole Polytechnique. Both authors have contributed to the establishment of results and the writing of the manuscript. J.H. has performed numerical calculations and K.L.H. has supervised the accuracy.

Competing interests

The authors declare no competing interests.

Additional information

Supplementary information The online version contains supplementary material available at <https://doi.org/10.1038/s42005-021-00641-0>.

Correspondence and requests for materials should be addressed to K.L.H.

Peer review information Communications Physics thanks the anonymous reviewers for their contribution to the peer review of this work. Peer reviewer reports are available.

Reprints and permission information is available at <http://www.nature.com/reprints>

Publisher's note Springer Nature remains neutral with regard to jurisdictional claims in published maps and institutional affiliations.



Open Access This article is licensed under a Creative Commons Attribution 4.0 International License, which permits use, sharing, adaptation, distribution and reproduction in any medium or format, as long as you give appropriate credit to the original author(s) and the source, provide a link to the Creative Commons license, and indicate if changes were made. The images or other third party material in this article are included in the article's Creative Commons license, unless indicated otherwise in a credit line to the material. If material is not included in the article's Creative Commons license and your intended use is not permitted by statutory regulation or exceeds the permitted use, you will need to obtain permission directly from the copyright holder. To view a copy of this license, visit <http://creativecommons.org/licenses/by/4.0/>.

© The Author(s) 2021, corrected publication 2021